INVITED ARTICLE

Electromagnetic interference shielding and mechanical properties of Si₃N₄–SiOC composites fabricated by 3D-printing combined with polymer infiltration and pyrolysis

Wenyan Duan, Zhe Fan, Hui Wang, Jingyi Zhang, Tianlu Qiao, and Xiaowei Yin[a),b)]
Science and Technology on Thermostructural Composite Materials Laboratory, Northwestern Polytechnical University, Xi'an 710072, China

Twinned silicon carbide (SiC) nanowires (NWs) reinforced Si₃N₄–SiOC composites were successfully fabricated through a joint process of three-dimensional printing (3DP), direct nitridation, and polymer infiltration and pyrolysis (PIP). 3DP and PIP were both addictive manufacturing processes, enabling the near net shape fabrication and microstructure designing of Si₃N₄–SiOC. With the increase of the PIP cycle number, the pores of Si₃N₄ were mostly filled with polymer-derived ceramics-silicon oxycarbide (containing SiC NWs and free carbons), which led to the increase of electrical conductivity of Si₃N₄–SiOC composites. With the increase of SiOC ceramics, the electromagnetic interference shielding effectiveness of Si₃N₄–SiOC composites increased from 2 dB to 35 dB, in which the absorption shielding effectiveness increased to 27 dB. The flexural strength of Si₃N₄–SiOC composites reached 63 MPa when the content of SiOC ceramics was 50.1 wt%. It is indicated that Si₃N₄–SiOC ceramics are a promising electromagnetic shielding and structural material.

I. INTRODUCTION

Recently, electromagnetic (EM) shielding materials have attracted wide attention due to their ability to protect the environment and sensitive devices from EM interference (EMI).[1–10] Compared with metal materials which cannot be used at high temperatures, ceramics are more suitable for EM shielding materials because of their excellent structural stability, oxidation resistance, creep resistance, and high-temperature mechanical properties.[11] EM shielding materials should have mobile charge carriers that can interact with the EM radiations.[12] They should contain carbon materials and nano-sized SiC, which have high electrical conductivity.[13–16] Therefore, many researches focus on EMI shielding effectiveness (SE) of Si–C–N based ceramics (Si₃N₄, SiC, C, SiO₂) and composites.[17] Usually, EMI SE is used to evaluate the capability of materials to shield the EM wave. As Eq. (1) shows, the total loss of the EMI shielding (SE$_T$) is composed of the reflection loss (SE$_R$), the absorption loss (SE$_A$), and multiple-

reflections SE loss (SE$_M$). In addition, SE$_M$ is negligible only if SE$_T$ > 15 dB,

$$SE_T = SE_R + SE_A + SE_M \quad . \tag{1}$$

Table I summarizes the SE of several typical Si–C–N based ceramics. It indicates that ceramics which contain insulating components and conductive phase are promising materials to block the EM radiation and eliminate the EMI microwave. Their conductivity and EMI SE can be easily adjusted and controlled by chemical approaches. Among these approaches, polymer infiltration and pyrolysis (PIP) is an efficient way to improve the electrical conductivity of ceramics by increasing the infiltration cycle.

Silicon based polymer-derived ceramics (PDCs) have obtained more attention because of their characterization that contains carbon materials and nano-sized SiC after heat-treatment.[23] Especially, SiC nanowires (NWs) and free carbons can be synthesized by pyrolysis of polysiloxane (PSO).[22] Porous silicon nitride (Si₃N₄) is selected as a matrix for its excellent mechanical properties, good oxidation resistance, and thermal-chemical corrosion resistance, which can be used in a harsh environment. Adding SiC NWs and free carbons into porous Si₃N₄ by PIP is an efficient way to prepare EMI shielding materials. Therefore, fabricating Si₃N₄–SiOC ceramics by PIP can create SiC NWs and free carbons in the pores to reduce the porosity and increase the density of the matrix, eventually making the Si₃N₄–SiOC ceramics with excellent EM shielding and high mechanical properties.

TABLE I. The comparison of EM shielding properties of different ceramics.

Materials	Matrix	Absorber	d (mm)	SE$_T$ (dB)	SE$_R$ (dB)	SE$_A$ (dB)	Ref.
CNTs–SiO$_2$	SiO$_2$	CNTs	5	33	…	…	18
C$_f$–SiO$_2$	SiO$_2$	C$_f$	2.5	12.1	…	…	2
Si$_3$N$_4$–PyC	Si$_3$N$_4$	PyC	2	13–13.5	3.8–5.7	7.5–8.6	19
Si$_3$N$_4$–CNTs	Si$_3$N$_4$	CNTs	1.5	30.5	8	22	20
Si$_3$N$_4$–SiC	Si$_3$N$_4$	SiC	2.8	27	6	21	21
SiC$_f$–SiC	SiC	PyC	2	28	27	1	15
PDC–SiOC	SiOC	SiC NWs, C	3	19	4	15	22
Si$_3$N$_4$–SiOC	Si$_3$N$_4$	SiC NWs, C	2	35	7	28	This work

Si$_3$N$_4$ can be fabricated by hot pressing and cold pressing followed by reactive sintering. All these technologies can only produce components with simple geometries. Compared with prior technologies, three-dimensional printing (3DP) is one special method of additive manufacturing. It can fabricate complex-shaped components without wasting materials. According to our previous researches, Si$_3$N$_4$ ceramics fabricated by 3DP and pressureless-sinter have an open porosity of 78%.[24] In order to further improve the mechanical properties of porous Si$_3$N$_4$ ceramics, direct nitridation of silicon is a promising way for the synthesis of Si$_3$N$_4$ ceramics. Compared with the previous work, the porosity of Si$_3$N$_4$ can be reduced by nearly 10% through direct nitridation of silicon.

In this paper, Si$_3$N$_4$–SiOC ceramics are synthesized by 3DP of silicon powders and direct nitridation of silicon, followed by PIP. It enables the complex-shape fabrication and microstructure designing and enhances EM shielding properties and mechanical properties of Si$_3$N$_4$–SiOC.

II. EXPERIMENT

The Si powder was mixed with Lu$_2$O$_3$ and dextrin powder with a mass ratio of 83:7:10. The mixed powder was ball-milled for 48 h in deionized water, and then dried at 80 °C for 24 h. The as-received powder blend was crushed and passed through a mesh sieve. The powder was printed into specimens with dimensions 3 × 10.5 × 24 mm^3 by 3DP, which was carried out in a 3D-printer (Spectrum Z510, Z Corporation, Rock Hill, South Carolina) using a water-based printer solution. During printing, the layer thickness was set to 0.0875 mm. Then the as-prepared specimens were decarburized at a temperature of 700 °C for 360 min. After this, the specimens were nitrided at 1500 °C for 120 min in the N$_2$ atmosphere in a tube furnace. The Si$_3$N$_4$ ceramics with a porosity of 70% were obtained.

PSO and 2 wt% ferrocene [Fe(C$_5$H$_5$)$_2$] were mixed for 30 min at 70 °C in the Ar atmosphere, and then a transparent orange liquid was obtained. The porous Si$_3$N$_4$ specimens were dipped into the obtained orange liquid for 30 min by a pressure infiltration process each time. The polymer in porous Si$_3$N$_4$ ceramics was cross-linked at 300 °C for 2 h and annealed at 1350 °C with a speed of 5 °C/min for 2 h with Ar gas as the protection atmosphere. The above processes were repeated several times until the desired content was reached. The obtained samples were designated as PIP-0, PIP-1, PIP-2, PIP-3, and PIP-4, respectively, corresponding to the infiltration cycles of 0, 1, 2, 3, and 4.

X-ray diffraction (XRD) was used for phase analysis (X'Pert Pro, Philips, Almelo, The Netherlands). INVIN Raman spectroscopy (RMS; Renishaw, Gloucestershire, United Kingdom) was used to characterize the graphitization degree of samples. The microstructure was observed by scanning electron microscopy (SEM; S-4700, Hitachi Corp., Tokyo, Japan) and transmission electron microscopy (TEM; G-20, FEI-Tecnai, Hillsboro, Oregon; at 300 kV). The scattering parameters (S-parameters, S_{11} and S_{21}) of each sample were measured by a vector network analyzer (VNA; MS4644A, Anritsu, Kanagawa, Japan) using the waveguide method in the X-band. The flexural strength was measured by a 3-point bending method on a universal testing machine (CMT 4304, Sans, Shenzhen, China) at a cross-head speed of 0.5 mm/min with a loading span of 30 mm.

III. RESULTS AND DISCUSSION

A. The microstructure of Si$_3$N$_4$–SiOC ceramics

Figure 1(a) shows XRD of Si$_3$N$_4$ (PIP-0) and Si$_3$N$_4$–SiOC. It is clearly indicated that the composites after the direct nitridation of silicon contain a high content of α-Si$_3$N$_4$, low content of β-Si$_3$N$_4$, and small amount of Si. The surface of the silicon nitride product is covered by long whiskers with a diameter in the micrometer range as shown in Fig. 2(a); it is indicated that the nitridation of silicon is related to the reaction in the gas phase. These whiskers are grown via a vaporization condensation type mechanism. Silicon vapor which generated from the surface reacted with nitrogen gas and deposited as Si$_3$N$_4$ whiskers.[25]

Si$_3$N$_4$–SiOC ceramics were successfully synthesized after the PIP process. The density and porosity of porous Si$_3$N$_4$ were 0.87 g/cm^3 and 70%, respectively. The density of porous Si$_3$N$_4$ after the nitridation of silicon was higher than that of Si$_3$N$_4$ prepared by 3DP and pressureless sintering of silicon nitride. After PIP, the weight gains of samples PIP-1 and PIP-2 were 33.4 wt% and 41.6%, the densities of samples PIP-1 and PIP-2 were 1.48 g/cm^3 and 1.72 g/cm^3, and porosities of samples PIP-1 and PIP-2 were 48 and 30%. As the infiltration cycle increased from three to four times, the weight gain of the porous Si$_3$N$_4$–SiC ceramic increased
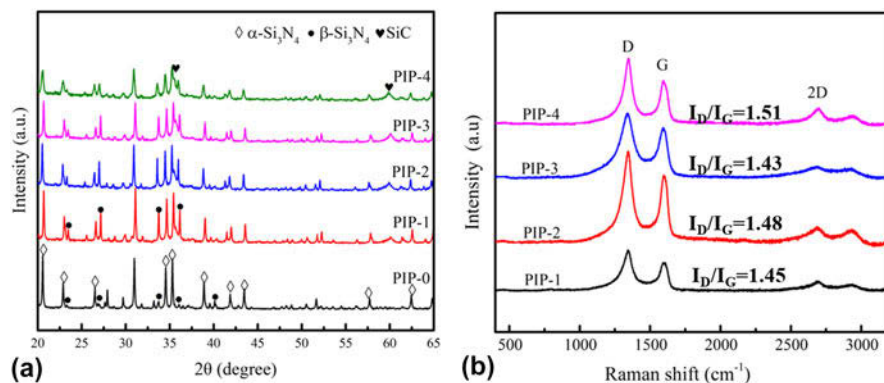
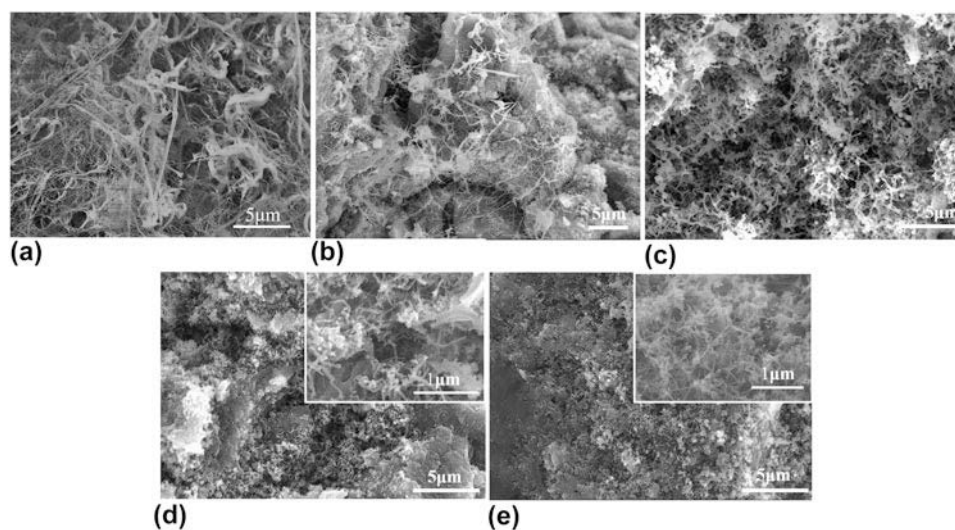FIG. 1. (a) XRD patterns and (b) Raman spectra of Si₃N₄–SiOC ceramics.

FIG. 2. SEM micrographs of the fracture surface of Si₃N₄–SiOC with different cycle numbers of PIP: (a) PIP-0, (b) PIP-1, (c) PIP-2, (d) PIP-3, and (e) PIP-4.

from 47.3 to 50.1 wt% with the density increasing gradually from 1.98 to 2.09 g/cm^3 and the total porosity decreasing slowly from 23 to 21%.

Figure 1(a) shows the XRD patterns of Si$_3$N$_4$–SiOC with dependence on the cycle number of PIP. The original porous Si$_3$N$_4$ ceramic was composed of α-Si$_3$N$_4$ and β-Si$_3$N$_4$. After infiltration, the crystalline peaks at 2θ of 23.4°, 27.1°, 33.7°, and 36.1° increased, referring to the diffraction from the (110), (200), (101), and (210) lattice planes of β-Si$_3$N$_4$, which suggested that some α-Si$_3$N$_4$ were transformed into β-Si$_3$N$_4$ during the process of PIP. In the meantime, all the samples showed the crystalline peaks at 35.6° and 60.0° after infiltration, which referred to the (111) and (220) lattice planes of β-SiC. With the increase of the infiltration cycle, the peak intensity of β-SiC increased gradually while the peak intensity of Si$_3$N$_4$ decreased, indicating that the content of SiC increased.

The Raman spectra of the samples are shown in Fig. 1(b). All the spectra of the samples showed the representative D band and G band, suggesting the existence of free carbons. The intensity ratio of the D band and G band, I_D/I_G, could

be used to evaluate the carbon cluster size. The I_D/I_G ratio of all samples after PIP, as shown in Fig. 1(b), had no remarkable change. The content of free carbons increased when the cycle number of PIP increased. The 2D band at about 2700 cm^{-1} is the overtone of the D band, which was sensitive to the stacking orders of graphene layers along the c axis. Therefore, the existence of the 2D band indicated the high crystallization of carbons.

Figure 2 shows the SEM micrographs of the fracture surface of Si$_3$N$_4$–SiOC ceramics with different cycle numbers of PIP. As shown in Fig. 2(b), SiC NWs with a diameter smaller than 100 nm were formed after the PIP process. With the increase of the cycle number of PIP, more SiC NWs were introduced into the porous ceramics. The porosity, as well as the size, of pores decreased.

Figure 3 shows the TEM images of the sample PIP-3. The interplanar spacing was 0.67 nm as shown in Fig. 3(a), corresponding to the (100) plane of Si$_3$N$_4$, which indicated that Si$_3$N$_4$ whiskers had already formed before the PIP process. There was some turbostratic carbon in the ceramics
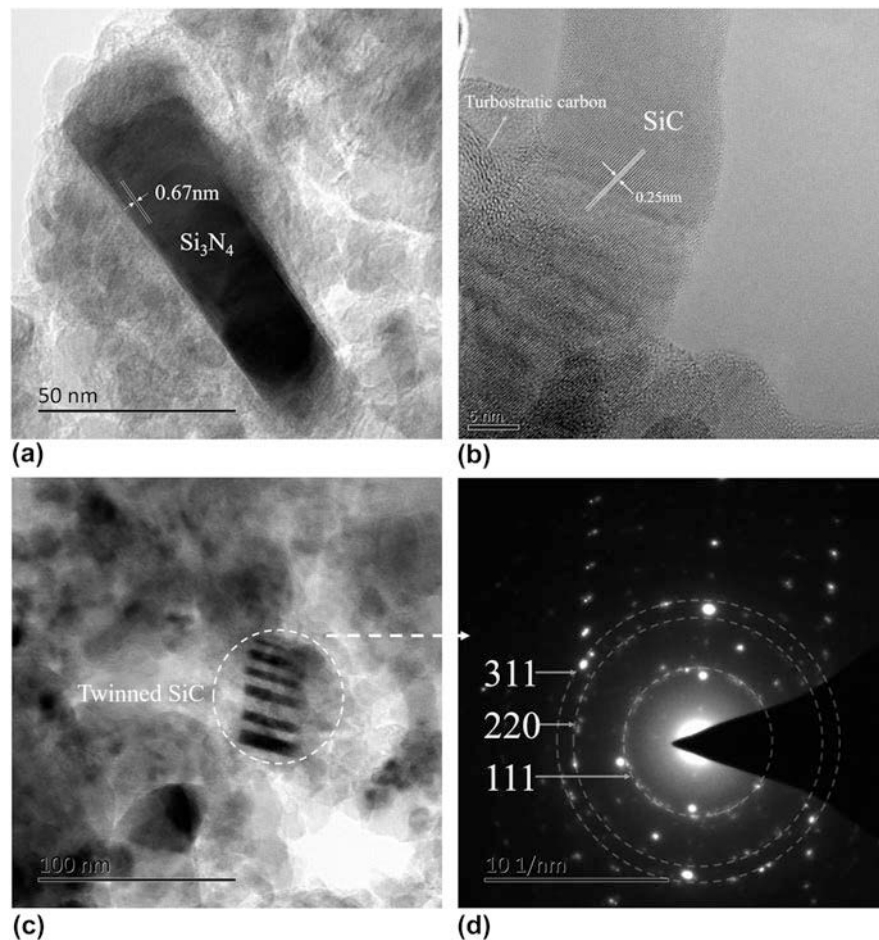
FIG. 3. TEM images of Si$_3$N$_4$–SiOC ceramics: (a) Si$_3$N$_4$, (b) turbostratic carbon, (c) twinned SiC nanowires, and (d) corresponding SAED.

as shown in Fig. 3(b). The TEM image [Fig. 3(c)] showed the existence of SiC NWs. The SiC NWs had a zigzag surface morphology. The selected area electron diffraction (SAED) pattern [Fig. 3(d)] showed three diffraction rings corresponding to the typical lattice planes of 3C–SiC. Besides diffraction rings, the diffraction spots gave two symmetrical sets of face-centered cubic lattices, suggesting that the zigzag part was composed of (111) twinning structures. The structures of twinned SiC NWs were similar to that in previous works.[26,27]

B. EMI shielding properties of Si$_3$N$_4$–SiOC ceramics

Figure 4 presents direct-current electrical conductivity (σ_{dc}) and EMI properties of Si$_3$N$_4$–SiOC ceramics. σ_{dc} of porous Si$_3$N$_4$ was 7.6×10^{-6} S/m. After PIP, the sample PIP-1 showed σ_{dc} of 3.6×10^{-1} S/m, indicating the formation of SiC NWs and turbostratic carbon played an important role in electrical conductivity. SiC NWs and carbon had high carrier concentration close to the metallic.[28] Therefore, the bridging and connectivity of SiC NWs in the pores and the existence of turbostratic carbon could

dramatically improve the electrical conductivity of Si$_3$N$_4$–SiOC ceramics. σ_{dc} of Si$_3$N$_4$–SiOC increased from 3.6×10^{-1} S/m to 45.3 S/m with the cycle number of PIP increasing from 1 to 4, which was attributed to the increase of the content of SiC NWs and turbostratic carbon.

As shown in Figs. 4(b)–4(d), SE$_R$ decreased and SE$_A$ increased with the frequency going up, which conformed to the trend of Eqs. (2) and (3) correctly. SE$_T$, SE$_A$, and SE$_R$ of samples all increased with the increase of the cycle number of PIP. The average SE$_T$, SE$_A$, and SE$_R$ of the samples increased from 2 to 35 dB, 0.1 to 28 dB, and 1 to 7 dB, respectively. SE$_A$ and SE$_R$ were closely associated with the frequency and the electrical conductivity according to Eqs. (2) and (3), respectively,[29]

$$SE_R = 39.5 + 10 \ \log \frac{\sigma}{2\pi f \mu} \quad , \quad (2)$$

$$SE_A = 8.7d\sqrt{\pi f \mu \sigma} \quad , \quad (3)$$

where f is the frequency, σ is the electric conductivity, μ is the permeability, and d is the specimen thickness.
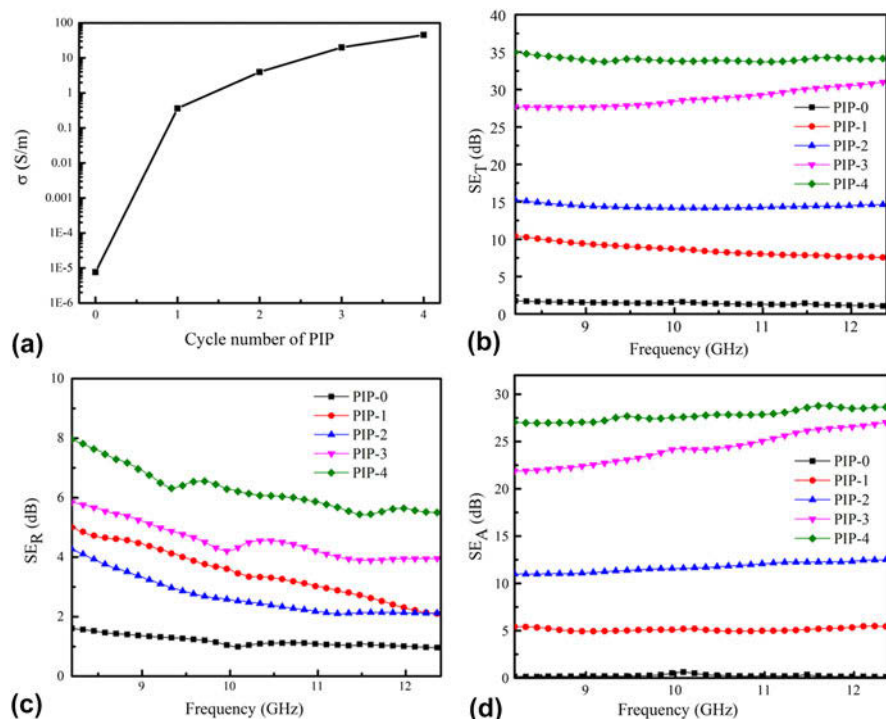
FIG. 4. (a) Electrical conductivity, (b) SE_T, (c) SE_R, and (d) SE_A of Si₃N₄–SiOC ceramics.

The schematic illustration of the shielding mechanism in Si₃N₄–SiOC ceramics is shown in Fig. 5. The increase of SE_R could be attributed to the formation of turbostratic carbon which leads to a high reflection of incident. Twinned SiC NWs with stacking fault and numerous dipoles formed in the pores could result in extensive polarization and energy dissipation.[16] SiC NWs possess a large surface area. A larger surface area of conductive material could give rise to interfacial polarization. Energy dissipation and interfacial polarization eventually lead to the increase of SE_A. SiC and carbon as the semiconductor and conductor make a great contribution to the absorption loss. Materials with low SE_R and high SE_A are candidates for EM absorption. The existence of Si₃N₄ and SiOC as microwave transparent materials could ensure the impedance match between free space and ceramics, which makes Si₃N₄–SiOC ceramics have a high SE_T of 35 dB with a lower SE_R of 7 dB and higher SE_A of 28 dB. It is indicated that more than 99.9% of the EM energy was reflected and absorbed and only less than 0.1% of the EM energy was transmitted.

C. Mechanical properties of Si₃N₄–SiOC ceramics

The flexural strength of Si₃N₄–SiOC ceramics with different cycle numbers of PIP was measured. After the direct nitridation of silicon, porous Si₃N₄ showed a low flexural strength (13 MPa) due to its high porosity and high content of α-Si₃N₄. After the infiltration cycle, the porosity of the sample PIP-1 decreased which would
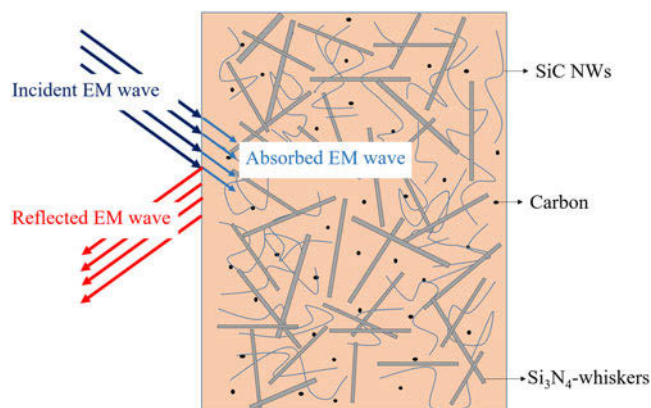

FIG. 5. Schematic illustration of the shielding mechanism in Si₃N₄–SiOC ceramics.

promote the increase of the flexural strength. The flexural strength of the sample PIP-1 was 37 MPa. When the infiltration cycle number was four times, the flexural strength of the sample PIP-4 increased to 63 MPa. Therefore, the increase of the content of SiOC enhanced the flexural strength of Si₃N₄–SiOC ceramics to a certain degree.

Table II offers present achievements in the field of processing of near-net-shaped 3D ceramic-based parts with a required shape using the 3DP technology.[24,30–32] 3DP can be used to create geometries that are difficult or impossible to create by traditional means.[33] The other advantage of 3DP is that there are no limitations on the

material species as long as it can be formulated into a powder which has good flowability and low internal friction. The drawback of 3DP is that ceramic-based parts have considerable porosity and require postprocessing. Sintering and infiltration are two most common postprocessing steps as shown in Table II. These steps can decrease the porosity and increase the flexural strength of ceramics. Si_3N_4–SiOC ceramics fabricated by 3DP and direct nitridation of silicon combined with PIP not only have high flexural strength but also possess excellent EMI shielding properties.

Figure 6 presents the computer-aided design model and the corresponding printed part composed of Si_3N_4 ceramics after the direct nitridation of silicon. The silicon nitride product has a linear shrinkage of 3–5%. It enables us to form components with accurate geometry dimension. This approach can also be used to print lattice truss structures, 3D mesh structures, and even more complex shapes.[34,35] What is more, it can also be further extended to develop other functional ceramic systems for electromagnetic wave (EMW) absorption and shielding applications.

TABLE II. Ceramic materials prepared by 3DP and corresponding properties.

| Raw materials for 3DP	Postprocessing	Result product	Dimensional change (%)	ρ (g/cm^3)	P (%)	σ_b (MPa)	SE_T (dB)	RC (dB)	Ref.
TiC, dextrin	Liquid silicon infiltration (LSI)	Ti_3SiC_2, SiC, TiC, $TiSi_2$	…	4.24	2.4	293 ± 17.8	…	…	31
TiC, TiO_2, dextrin	Reactive Al-melt infiltration	Ti_3AlC_2, $TiAl_3$, Al_2O_3	1.5–3.2	3.4	1.7	320 ± 40	…	…	30
C, catalyst, resin	Reaction infiltration	Si, SiC	22	0.83	28	…	…	…	32
Si, SiC, dextrin	PIP	Si, SiC	3–4	2.74	0.5	208 ± 25	…	…	34
Si_3N_4, Lu_2O_3, dextrin	Pressureless-sintering + PIP	Si_3N_4, SiC	…	1.78	34	…	…	−57	24
Si, Lu_2O_3, dextrin	Direct nitridation of silicon + PIP	Si_3N_4, SiC, C	3–5	2.09	21	63 ± 8	35	…	This work
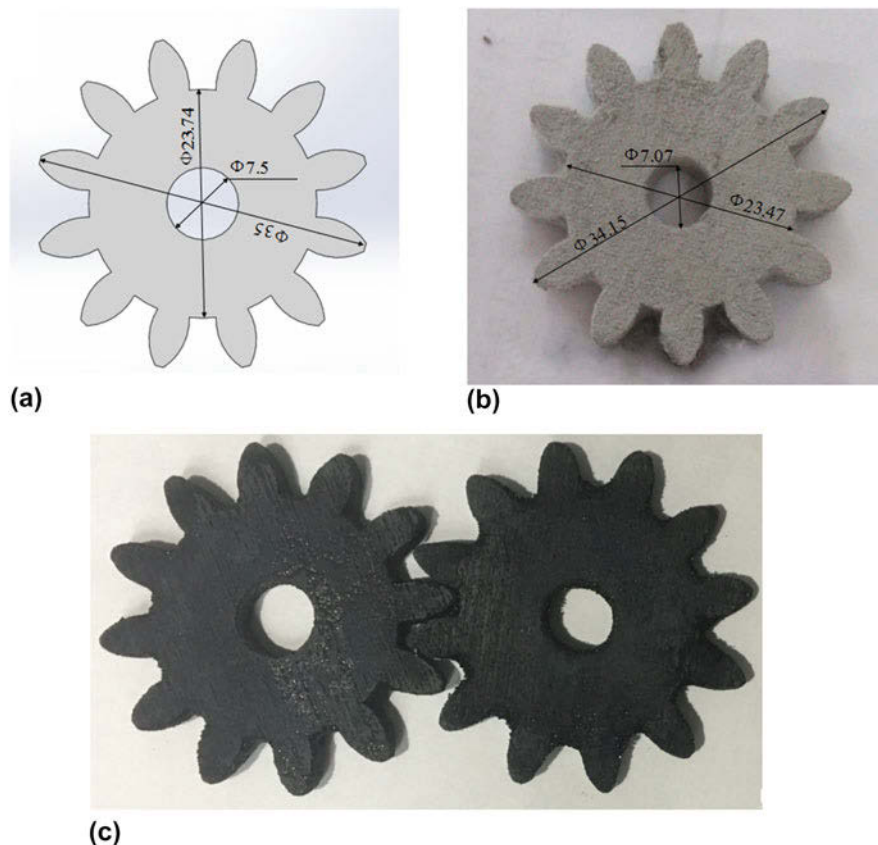
FIG. 6. (a) Computer-aided design model, (b) corresponding porous Si_3N_4 after the direct nitridation of silicon, and (c) Si_3N_4–SiOC ceramics with a complex shape.

IV. CONCLUSION

In this study, PDC–SiOC which contained SiC NWs and free carbons was *in situ* formed in porous Si$_3$N$_4$ ceramics by the PIP process. With the increase of the infiltration cycle number, most of the pores were filled with SiC NWs and free carbons, which acted as the conductive phase and reinforced phase, resulting in the improvement of both shielding and mechanical properties. As the porosity went down from 70 to 21%, the average SE_T rose from 2 dB to 35 dB with a lower SE_R of 7 dB and higher SE_A of 28 dB, and the flexural stress reached 63 Mpa. Therefore, it is demonstrated that the SiC NWs reinforced Si$_3$N$_4$–SiOC ceramics are a promising EM shielding and structural material. The method in this work can be further extended to prepare other functional ceramic systems with a complex shape.

ACKNOWLEDGMENT

REFERENCES

1. X. Yin, L. Kong, L. Zhang, L. Cheng, N. Travitzky, and P. Greil: Electromagnetic properties of SiCN based ceramics and composites. *Int. Mater. Rev.* **59**(6), 326 (2014).

2. M.S. Cao, W.L. Song, Z.L. Hou, B. Wen, and J. Yuan: The effects of temperature and frequency on the dielectric properties, electromagnetic interference shielding and microwave-absorption of short carbon fiber/silica composites. *Carbon* **48**(3), 788 (2010).

3. B. Fugetsu, E. Sano, M. Sunada, Y. Sambongi, T. Shibuya, X. Wang, and T. Hiraki: Electrical conductivity and electromagnetic interference shielding efficiency of carbon nanotube/cellulose composite paper. *Carbon* **46**(9), 1256 (2008).

4. D. Micheli, C. Apollo, R. Pastore, and M. Marchetti: X-Band microwave characterization of carbon-based nanocomposite material, absorption capability comparison and RAS design simulation. *Compos. Sci. Technol.* **70**(2), 400 (2010).

5. C. Brosseau: Modelling and simulation of dielectric heterostructures: A physical survey from an historical perspective. *J. Phys. D: Appl. Phys.* **39**, 1277 (2006).

6. L. Kong, Z. Li, L. Liu, R. Huang, M. Abshinova, Z. Yang, C. Tang, P. Tan, C. Deng, and S. Matitsine: Recent progress in some composite materials and structures for specific electromagnetic applications. *Int. Mater. Rev.* **58**(4), 203 (2013).

7. Z.C. Shi, R.H. Fan, Z.D. Zhang, L. Qian, M. Gao, M. Zhang, L.T. Zheng, X.H. Zhang, and L.W. Yin: Random composites of nickel networks supported by porous alumina toward double negative materials. *Adv. Mater.* **24**(17), 2349 (2012).

8. K. Sun, R. Fan, Z. Zhang, K. Yan, X. Zhang, P. Xie, M. Yu, and S. Pan: The tunable negative permittivity and negative permeability of percolative Fe/Al₂O₃ composites in radio frequency range. *Appl. Phys. Lett.* **106**(17), 172902 (2015).

9. Z. Wang, L. Wu, J. Zhou, Z. Jiang, and B. Shen: Chemoselectivity-induced multiple interfaces in MWCNT/Fe₃O₄@ZnO heterotrimers for whole X-band microwave absorption. *Nanoscale* **6**(21), 12298 (2014).

10. C. Liang, Y. Gou, L. Wu, J. Zhou, Z. Kang, B. Shen, and Z. Wang: Nature of electromagnetic-transparent SiO₂ shell in hybrid nanostructure enhancing electromagnetic attenuation. *J. Phys. Chem. C* **120**(24), 12967 (2016).

11. F.L. Riley: Silicon nitride and related materials. *J. Am. Ceram. Soc.* **83**(2), 245 (2000).

12. D. Chung: Carbon materials for structural self-sensing, electromagnetic shielding and thermal interfacing. *Carbon* **50**(9), 3342 (2012).

13. F. Moglie, D. Micheli, S. Laurenzi, M. Marchetti, and V.M. Primiani: Electromagnetic shielding performance of carbon foams. *Carbon* **50**(5), 1972 (2012).

14. Y. Mu, W. Zhou, C. Wang, F. Luo, D. Zhu, and D. Ding: Mechanical and electromagnetic shielding properties of SiC$_f$/SiC composites fabricated by combined CVI and PIP process. *Ceram. Int.* **40**(7), 10037 (2014).

15. D. Ding, Y. Shi, Z. Wu, W. Zhou, F. Luo, and J. Chen: Electromagnetic interference shielding and dielectric properties of SiC$_f$/SiC composites containing pyrolytic carbon interphase. *Carbon* **60**, 552 (2013).

16. H. Zhang, Y. Xu, J. Zhou, J. Jiao, Y. Chen, H. Wang, C. Liu, Z. Jiang, and Z. Wang: Stacking fault and unoccupied densities of state dependence of electromagnetic wave absorption in SiC nanowires. *J. Mater. Chem. C* **3**(17), 4416 (2015).

17. C. Cheng, K. Yan, R. Fan, L. Qian, Z. Zhang, K. Sun, and M. Chen: Negative permittivity behavior in the carbon/silicon nitride composites prepared by impregnation-carbonization approach. *Carbon* **96**, 678 (2016).

18. C. Xiang, Y. Pan, X. Liu, X. Sun, X. Shi, and J. Guo: Microwave attenuation of multiwalled carbon nanotube-fused silica composites. *Appl. Phys. Lett.* **87**(12), 123103 (2005).

19. X. Hao, X. Yin, L. Zhang, and L. Cheng: Dielectric, electromagnetic interference shielding and absorption properties of Si₃N₄–PyC composite ceramics. *J. Mater. Sci. Technol.* **29**(3), 249 (2013).

20. M. Chen, X. Yin, M. Li, L. Chen, L. Cheng, and L. Zhang: Electromagnetic interference shielding properties of silicon nitride ceramics reinforced by *in situ* grown carbon nanotubes. *Ceram. Int.* **41**(2), 2467 (2015).

21. X. Li, L. Zhang, X. Yin, L. Feng, and Q. Li: Effect of chemical vapor infiltration of SiC on the mechanical and electromagnetic properties of Si₃N₄–SiC ceramic. *Scr. Mater.* **63**(6), 657 (2010).

22. W. Duan, X. Yin, Q. Li, X. Liu, L. Cheng, and L. Zhang: Synthesis and microwave absorption properties of SiC nanowires reinforced SiOC ceramic. *J. Eur. Ceram. Soc.* **34**(2), 257 (2014).

23. P. Colombo, G. Mera, R. Riedel, and G.D. Sorarù: Polymer-derived ceramics: 40 years of research and innovation in advanced ceramics. *J. Am. Ceram. Soc.* **93**(7), 1805 (2010).

24. W. Duan, X. Yin, F. Cao, Y. Jia, Y. Xie, P. Greil, and N. Travitzky: Absorption properties of twinned SiC nanowires reinforced Si₃N₄ composites fabricated by 3d-prining. *Mater. Lett.* **159**, 257 (2015).

25. V. Pavarajarn, T. Vongthavorn, and P. Praserthdam: Enhancement of direct nitridation of silicon by common metals in silicon nitride processing. *Ceram. Int.* **33**(4), 675 (2007).

26. R. Wu, Y. Pan, G. Yang, M. Gao, L. Wu, J. Chen, R. Zhai, and J. Lin: Twinned SiC zigzag nanoneedles. *J. Phys. Chem. C* **111**(17), 6233 (2007).

27. Z. Lin, L. Wang, J. Zhang, X.Y. Guo, W. Yang, H.K. Mao, and Y. Zhao: Nanoscale twinning-induced elastic strengthening in silicon carbide nanowires. *Scr. Mater.* **63**(10), 981 (2010).

28. H.K. Seong, H.J. Choi, S.K. Lee, J.I. Lee, and D.J. Choi: Optical and electrical transport properties in silicon carbide nanowires. *Appl. Phys. Lett.* **85**(7), 1256 (2004).

29. S. Celozzi, G. Lovat, and R. Araneo: *Electromagnetic shielding* (Wiley, Hoboken, 2008).
30. X. Yin, N. Travitzky, and P. Greil: Near-net-shape fabrication of Ti₃AlC₂-based composites. *Int. J. Appl. Ceram. Technol.* **4**(2), 184 (2007).
31. B. Nan, X. Yin, L. Zhang, and L. Cheng: Three-dimensional printing of Ti₃AlC₂-based ceramics. *J. Am. Ceram. Soc.* **94**(4), 969 (2011).
32. J. Moon, A.C. Caballero, L. Hozer, Y.M. Chiang, and M.J. Cima: Fabrication of functionally graded reaction infiltrated SiC–Si composite by three-dimensional printing (3DP™) process. *Mater. Sci. Eng., A* **298**(1), 110 (2001).
33. B. Utela, D. Storti, R. Anderson, and M. Ganter: A review of process development steps for new material systems in three dimensional printing (3DP). *J. Manuf. Process.* **10**(2), 96 (2008).
34. Z. Fu, L. Schlier, N. Travitzky, and P. Greil: Three-dimensional printing of SiSiC lattice truss structures. *Mater. Sci. Eng., A* **560**, 851 (2013).
35. K. Lu and W.T. Reynolds: 3DP process for fine mesh structure printing. *Powder Technol.* **187**(1), 11 (2008).